Check for updates

ADVANCED FUNCTIONAL MATERIALS
www.afm-journal.de

Tunable Linear Weight Modulation via Ion Dynamics in Electrolyte-Gated Synaptic Transistors: Molecular Dynamics and Experimental Insights into Ion Concentration Effects

Haeyeon Lee, Sobin Alosious, Minho Jin, Yeonseo Kim, Tengfei Luo, and Youn Sang Kim**

Electrolyte-gated transistors (EGTs) are promising candidates for low-power and energy-efficient artificial synapses utilizing rapid ion-mediated electrostatic and electrochemical reactions. However, the correlation between sub-nanosecond ion transport and linear conductance modulation remains elusive when analyzed solely by macroscopic electrical characterization. Here, molecular dynamics (MD) simulations are integrated with experiments using Li-EGTs at different ion concentrations. MD simulations quantify Li^+ displacement, coordination environments, and ionic conductivity in poly(ethylene oxide) electrolytes, revealing suppressed Li^+ diffusivity and reorganization of the ethylene oxide (EO) solvation structure at an [EO]:[Li^+] ratio of 8:1. EGTs are fabricated with different EO ratios to investigate the transition regime. Electrochemical impedance spectroscopy, optical microscopy, and X-ray diffraction confirm the MD-predicted ion dynamic transition at 8:1 EO ratio and identify phase crystallization at the ultrahigh 2:1 ratio. Consequently, Li-EGTs fabricated with the optimized 2:1 EO ratio successfully achieve an accuracy of 89.51% in neural network training. This study bridges atomic-scale insights and device performance, offering a systematic, precision-engineered framework for complex spatiotemporal ion dynamics in artificial synaptic EGTs.

1. Introduction

Inspired by the parallel and interconnected architecture of the biological nervous system, neuromorphic devices have been developed to efficiently perform data-intensive tasks with low power consumption.[1,2] These devices emulate essential synaptic functions, such as short-term and long-term plasticity, paired-pulse facilitation (PPF), and long-term potentiation/depression (LTP/LTD) through electrical stimuli.[3] To date, extensive research has been conducted on developing synaptic devices configured in both two-terminal and three-terminal architectures.[4–6] Among them, electrolyte-gated transistors (EGTs) have attracted significant attention due to notable advantages, such as large areal capacitance, ultra-low power consumption, precise conductance controllability, and compatibility with flexible substrates.[7,8] These advantages stem from the operational mechanism of EGTs, where mobile ions within the electrolyte migrate toward the channel or electrode interface in response to the applied gate voltage. This forms a nanometer-thick electric double layer (EDL) at the interface, which induces a high gate capacitance through strong electrostatic coupling with the channel layer and facilitates low-voltage and power-efficient operation.[9] Therefore, it is necessary to elucidate the reaction kinetics and ion transport mechanisms governing synaptic functions for the advancement of EGTs.

H. Lee, Y. Kim, Y. S. Kim
Department of Chemical and Biological Engineering
Seoul National University
Gwanak-ro 1, Gwanak-gu, Seoul 08826, Republic of Korea
E-mail: younskim@snu.ac.kr

Y. S. Kim
Institute of Chemical Processes
Seoul National University
Gwanak-ro 1, Gwanak-gu, Seoul 08826, Republic of Korea

M. Jin, Y. S. Kim
Program in Nano Science and Technology
Graduate School of Convergence Science and Technology
Seoul National University
Gwanak-ro 1, Gwanak-gu, Seoul 08826, Republic of Korea

The ORCID identification number(s) for the author(s) of this article can be found under https://doi.org/10.1002/adfm.202517100

S. Alosious, T. Luo
Lucy Family Institute for Data and Society
University of Notre Dame
Notre Dame, IN 46556, USA
E-mail: tluo@nd.edu

S. Alosious, T. Luo
Department of Aerospace and Mechanical Engineering
University of Notre Dame
Notre Dame, IN 46556, USA

T. Luo
Center for Sustainable Energy (ND Energy)
University of Notre Dame
Notre Dame, IN 46556, USA

T. Luo
Department of Chemical and Biomolecular Engineering
University of Notre Dame
Notre Dame, IN 46556, USA

DOI: 10.1002/adfm.202517100

 © 2025 Wiley-VCH GmbH

Previous studies have reported various working mechanisms of synaptic devices using functional ions (H^+, Li^+, Na^+, K^+, and $EMIM^+$) in EGTs, including electrochemical doping, ion trapping, intercalation, and dipole alignment in ferroelectric materials.[10–15] We have previously revealed that nonvolatile memory characteristics in poly(ethylene oxide) (PEO)-based EGTs originate from interfacial reactions at the electrolyte/semiconductor interface, where faradaic redox reactions of Li^+ enhance memory retention compared to EDL effects.[16] Conversely, the linearity and symmetry of conductance modulation are governed by ion dynamics within the bulk polymer electrolyte, with crystallized K-PEO systems enabling more linear and symmetric updates via a hopping mechanism that involves a higher activation energy barrier.[16] However, macroscopic electrical measurements cannot fully resolve sub-nanosecond atomic motions, such as the trajectories of ions and their interactions with ethylene oxide (EO) groups.[17] On the other hand, while previous computational studies have investigated Li^+ dynamics in water-in-salt (WiS) systems, there's a fundamental difference in transport mechanism with polymer systems: WiS allows rapid Li^+ hopping via liquid water on nanosecond timescales, whereas solid PEO relies on slower polymer segmental relaxation requiring tens to hundreds of nanoseconds.[18] In particular, WiS electrolytes face additional limitations, including large variations in solubility limits by ion species and strict operational voltage constraints due to water decomposition (ESW $\leq$ 1.23 V).[19] Consequently, most studies have relied on either macroscopic measurements or simplified models that do not directly reflect device-relevant conditions. Nevertheless, Li^+ remains widely used in electronic devices due to its cost-effectiveness, high solubility for efficient ion transport, long-term cycling stability, and broad compatibility with various materials.[20–22] Therefore, to efficiently analyze synaptic characteristics using Li^+ while minimizing time, effort, and material use, computational analysis integrated with experimental validation is essential for elucidating fine-scale ion transport and structural behavior.

Here, we employ an integrated framework combining molecular dynamics (MD) simulations and experiments to investigate Li^+ dynamics and solvation structures in PEO as a function of ion concentration. Using MD simulations, we track Li^+ trajectories at six different [EO]:[Li^+] ratios from 50:1 to 2:1, with long PEO chains (N = 100) to suppress finite-size effects and faithfully reproduce real EGT environments. Femtosecond-resolved trajectories capture ion transport and solvation structures under experimentally relevant EO ratios, quantified via mean square displacement (MSD), radial distribution function (RDF), and polymer radius of gyration (R_g). This carefully designed simulation framework directly bridges atomic-scale dynamics with device-level behavior, extending beyond prior MD studies confined to bulk electrolyte analysis. Corresponding lithium bis(trifluoromethanesulfonyl)imide (LiTFSI)/PEO electrolytes (10:1, 8:1, 5:1, and 2:1) are synthesized and characterized using optical microscopy (OM), X-ray diffraction (XRD), and electrochemical impedance spectroscopy (EIS) to correlate polymer conformation and ionic conductivity with simulation results. All EGTs exhibit wide memory windows exceeding 3 V. Notably, the device at a 2:1 EO ratio achieves pronounced multilevel conductance modulation with nonlinearity (NL) factors of 0.42 (potentiation) and −0.50 (depression), which demonstrate 89.51% accuracy in neural network training. Our multiscale strategy effectively bridges atomic-level ion dynamics with macroscopic device performance, offering valuable insights for the development of advanced artificial synaptic EGTs.

2. Results and Discussion

2.1. Identification of Coordination Structures of PEO/LiTFSI Electrolytes by MD Simulation

Figure 1a illustrates a 3D schematic of an EGT with a side-gate geometry. A solid polymer electrolyte (SPE), composed of PEO and LiTFSI, serves as the dielectric and is deposited atop a thin-film ZnO semiconductor channel. Based on this configuration, MD simulations examine the electrolyte's conformational arrangements and the associated ion dynamics across varying ion concentrations using the Large-scale Atomic/Molecular Massively Parallel Simulator (LAMMPS) software package. The all-atom optimized potentials for liquid simulations–all-atom (OPLS-AA) force field was used. As shown in Figure 1b, the simulation box comprises ten methyl-terminated PEO chains of 100 monomers each (Mn = 4705.7 g mol^{-1}), a chain length above the ≈ 4 kg mol^{-1} threshold at which Li^+ self-diffusion coefficients (D) and ionic conductivities in PEO/LiTFSI electrolytes plateau, making 100-mer chains comparable to the long-chain PEO used experimentally (Mn ≈100 kg mol^{-1}). Therefore, this MD model should be able to faithfully model the long-chain ion-transport regime without introducing finite-size artifacts.[23,24] We study six ion concentrations corresponding to [EO]:[Li^+] ratios (EO ratio) of 50:1, 25:1, 10:1, 8:1, 5:1, and 2:1. These EO ratios represent standard concentrations widely investigated in PEO-based electrolyte studies, spanning from dilute to concentrated regimes and encompassing the experimentally observed optimal range for ionic conductivity.[25–27] Therefore, we selected these six conditions to systematically investigate the transitions in physicochemical properties, coordination structures, and ion transport mechanisms as a function of ion concentration.

We employed the OPLS-AA force field to model the bonded (bond stretching, angle bending, torsional) and nonbonded (Lennard-Jones and Coulombic) interactions of PEO, Li^+, and $TFSI^-$ (Figure S1, Supporting Information). The OPLS-AA force field parameters for both PEO and LiTFSI were generated using Moltemplate.[28] For LiTFSI, however, we replaced the standard OPLS-AA partial charges with those reported by Jiang et al., which have been shown to yield more accurate ionic interactions (Table S1, Supporting Information).[29] The OPLS-AA framework has been extensively validated and appropriately applied to a wide range of polymer–electrolyte systems, demonstrating its reliability in modeling ion–polymer dynamics.[25,30–32] Nonetheless, as a non-polarizable force field, the OPLS-AA force field does not explicitly include polarization or charge transfer between ions and their surroundings. Ab initio studies have shown that, in condensed phases, ionic net charges are effectively reduced due to these effects.[33–35] In classical MD, this is often mimicked by scaling down the partial charges, which improves agreement with experiments in some cases. However, this approach may not fully account for the dynamic and local fluctuations in polarization, which become more significant at high salt concentrations. Therefore, while our simulations capture qualitative trends in

© 2025 Wiley-VCH GmbH

16163028, 2026, 24, Downloaded from https://advanced.onlinelibrary.wiley.com/doi/10.1002/adfm.202517100 by University Of Notre Dame, Wiley Online Library on [11/07/2026]. See the Terms and Conditions (https://onlinelibrary.wiley.com/terms-and-conditions) on Wiley Online Library for rules of use; OA articles are governed by the applicable Creative Commons License

16163028, 2026, 24, Downloaded from https://advanced.onlinelibrary.wiley.com/doi/10.1002/adfm.202517100 by University Of Notre Dame, Wiley Online Library on [11/07/2026]. See the Terms and Conditions (https://onlinelibrary.wiley.com/terms-and-conditions) on Wiley Online Library for rules of use; OA articles are governed by the applicable Creative Commons License

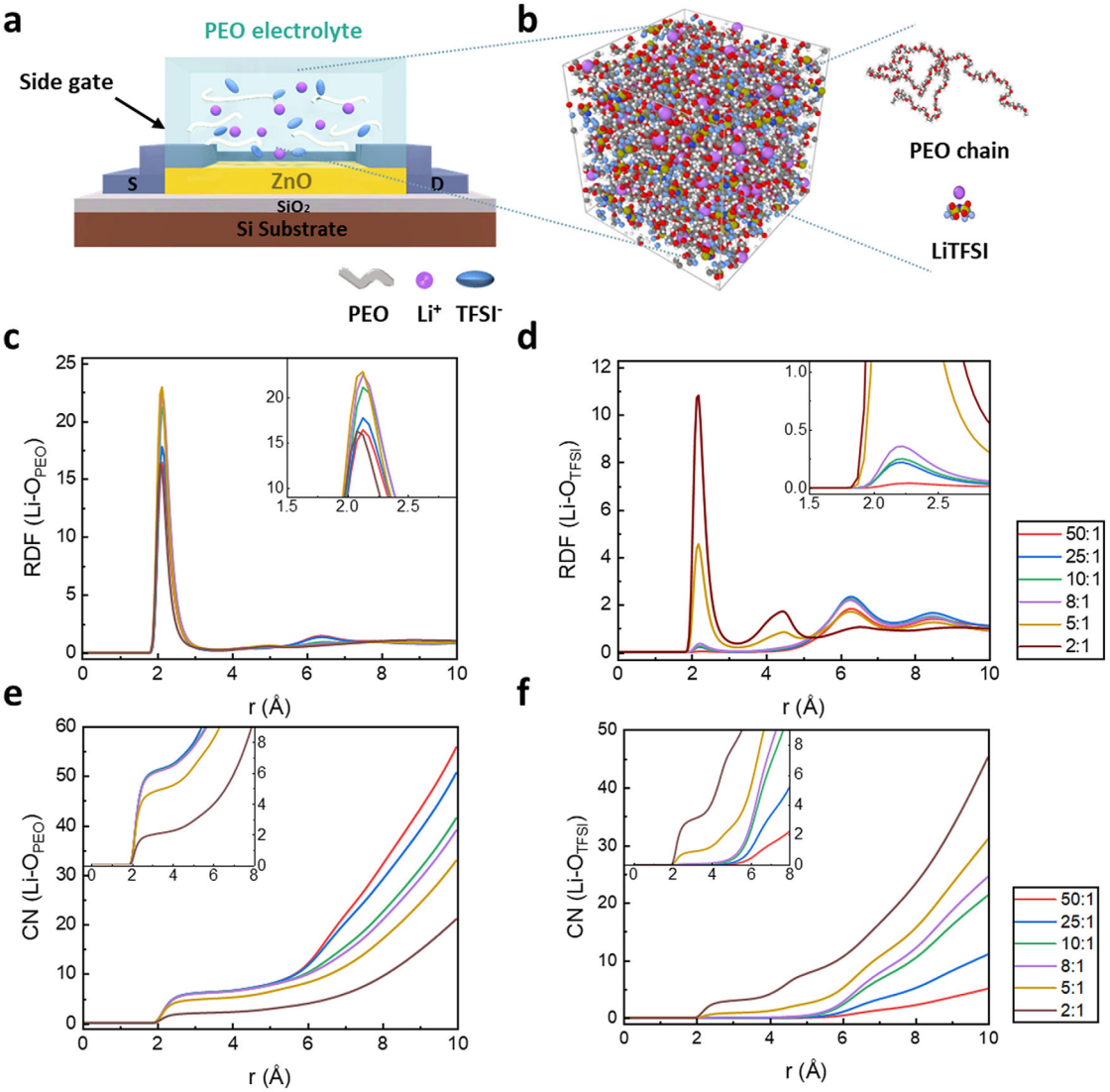


Figure 1. 3D illustration of Li-EGT, including MD simulation snapshot and Li^+ solvation structure in PEO electrolytes. a) Schematic of a side-gate Li-EGT with a PEO/LiTFSISPE film covering the gate, source, and drain electrodes on a $Si/SiO_2/ZnO$ substrate. b) Snapshot of the MD simulation box of the PEO/LiTFSI system, showing the distribution of polymer chains and ionic species. Insets depict a representative PEO chain ($N = 100$) and a LiTFSI ion pair. Representative RDFs between c) Li^+ ions and PEO oxygen atoms, and d) between Li^+ ions and $TFSI^-$ oxygen atoms for various EO ratios ranging from 50:1 to 2:1. Insets show the strong Li—O peaks at 1.5–2.9 Å observed within the first solvation shell of Li^+ ions. Distribution of CNs between e) Li^+ ions and PEO oxygen atoms, and f) between Li^+ ions and $TFSI^-$ oxygen atoms for various EO ratios ranging from 50:1 to 2:1. Insets show a magnified view of the CN evolution related to the effect of salt concentration on the initial coordination environment of Li^+.

coordination and conductivity, the quantitative results, especially at high concentrations, should be interpreted with this limitation in mind.

Before calculating the material properties at different ion concentrations, we first validated the simulation setup by calculating glass transition temperatures (T_g) of two representative electrolyte systems—pure PEO and the 8:1 EO ratio—using MD simulations. The T_g values were determined by the intersection point of two linear regressions fitted to the high- and low-temperature regions of the density-temperature (ρ–T) curve and compared with experimental DSC values.[36] The MD-calculated T_g values—237.8 K (−35.3 °C) for pure PEO and 222.4 K (−50.7 °C) for the 8:1 EO ratio—showed deviations of 11.6 °C and 4.9 °C from the experimental DSC values of −23.7 °C and −45.8 °C, respectively.[16] Such underestimation is attributed to i) the slightly lower simulated densities compared to experiment (1.13 g mL^{-1} at 25 °C), which increase free volume and chain mobility, and ii) the intrinsic approximations of the force field. Nevertheless, these deviations are within acceptable ranges, demonstrating that our simulations accurately reproduce the thermal behavior and characteristics of long-chain PEO (M_w = 100 000 g mol^{-1}). The detailed calculation procedure is provided in the supporting information (Figure S2 and Note, Supporting Information).

First, the RDF and coordination number (CN) were computed to verify the solvation states of Li^+ in the PEO/LiTFSI electrolyte

 © 2025 Wiley-VCH GmbH

at different ion concentrations. In the RDF, each peak's position quantitatively defines the characteristic interaction distance between the selected species, while the corresponding peak intensity reflects the degree of association. Figure 1c,d indicates the RDF of target oxygen atoms from PEO and $TFSI^-$, respectively, around the reference Li^+ ions as a function of radial distance. The first peak, located at 2.125 Å for $Li—O_{PEO}$ and at 2.175 Å $Li—O_{TFSI}$, corresponds to the average distance between Li^+ and the coordinating oxygen atoms within the first coordination shell. The Li—O RDF peaks at 2.125 and 2.175 Å are very close to the sum of ionic radii for Li^+ (0.76 Å) and O^{2-} (1.40 Å), and also agree with neutron scattering measurements at 296 K, thus confirming the direct Li—O coordination.[37,38] The increase in the first peak intensity, as the ion concentration rises from 50:1 to 8:1, can be attributed to the enhanced local coordination of Li^+ with the surrounding PEO oxygen atoms (Figure 1c). As the Li^+ concentration increases, the probability of free Li^+ interacting with nearby oxygen atoms of PEO rises, leading to a higher local number density.

However, when the EO ratio exceeds 8:1, the first-peak intensity saturates, indicating that at this concentration, all coordination sites between Li^+ and EO are fully occupied. At an ultrahigh 2:1 ratio, the first-peak intensity decreases, as overcrowding reduces the number of oxygen atoms available to coordinate each Li^+, thereby lowering the local coordination density. Meanwhile, the RDF for $Li—O_{TFSI}$ interactions within the first solvation shell ($r < 3.6$ Å) begins to exhibit a distinct coordination peak at 5:1 and 2:1 ratios, reflecting competitive solvation between the ethylene oxide and $TFSI^-$ accompanied by the simultaneous formation of ion-pairs and clusters. At the low concentration regime (from 50:1 to 8:1 ratios), only a slight increase in peak intensity is observed, and the distribution remains bimodal with a dominant peak at 6.2 Å, suggesting that Li^+ remains largely dissociated from $TFSI^-$ up to 8:1 ratio.[24,39]

We further analyzed the CN distribution, which is the integrated RDF up to the first minimum radius calculated with the following Equation (1),

$$N_a = 4\pi n_b \int_0^{R_M} g_{ab}(r)\, r^2 dr \quad (1)$$

where R_M is the radial distance of the first minimum after the first peak in RDF, g_{ab}, and n_b is the number density of b atoms.[40] Figure 1e,f shows that each Li^+ ion was coordinated by an average of six oxygen atoms, all originating from PEO chains, up to the 8:1 ratio. However, at a 5:1 ratio, one Li^+ is coordinated with an average of 5 oxygen atoms from PEO and 1 from $TFSI^-$, indicating the existence of ion pairs at high concentration. An ultrahigh EO ratio of 2:1, Li^+ coordinates with an average of only 2 oxygen atoms from PEO, while the CN with $TFSI^-$ increases to 4. These RDF and CN analyses indicate that Li^+ ions, fully dissociated at lower concentrations, begin forming ion pairs and predominantly exist as ion pairs or clusters from a 5:1 EO ratio under super-concentrated conditions. These simulation results suggest that a transition in the coordination environment due to ion concentrations has the potential to significantly impact Li^+ transport mechanisms.

2.2. Investigation of Li^+ Dynamics and Morphology of PEO/LiTFSI Electrolytes by MD Simulation

Changes in Li^+-polymer coordination and ion-ion association significantly affect ion migration properties. Therefore, the MSD and D of Li^+ and $TFSI^-$ at varying ion concentrations were calculated using the MSD relation, averaged over 5 independent simulations, as shown in Figure S23 (Supporting Information) (details are in the Experimental Section). The MSD calculation was performed with respect to the center of mass of the target molecule to remove overall translation and rotation, investigating intrinsic diffusion.[41,42] As shown in **Figure 2a**, particles exhibited sub-diffusive behavior during the initial production run, characterized by a nonlinear MSD–time relationship with a slope less than one.[43] As the simulation progressed, the system entered the diffusive regime, where MSD increased linearly with time. The MSD values at 50 ns revealed a clear dependence of Li^+ displacement on the EO ratio. At dilute concentration (50:1), the MSD reaches its maximum (28.71 $Å^2$). With increasing salt content, the MSD decreases and then exhibits a plateau between 25:1 (25.22 $Å^2$) and 15:1 (25.11 $Å^2$). Beyond this region, the MSD drops markedly, reaching 15.19 $Å^2$ at 8:1 and 11.08 $Å^2$ at 5:1.

In the low Li^+ content regime (from 50:1 to 8:1), the MSD reaches its maximum at the lowest concentration (50:1). Then, Li^+ displacement decreases monotonically and exhibits a plateau between 25:1 and 8:1 EO ratios. The final displacement values at 50 ns are 28.71 $Å^2$ (50:1), 25.22 $Å^2$ (25:1), 25.37 $Å^2$ (10:1), and 25.11 $Å^2$ (8:1), indicating saturation behavior of Li^+ near the intermediate concentration. However, beyond the 8:1 ratio, the MSD values at 50 20 ns markedly decrease to 15.19 $Å^2$ and 11.08 $Å^2$ for the 5:1 and 2:1 EO ratios, respectively, in the concentrated regime. This reduction suggests that increasing ion concentration leads to constrained ion motion, likely due to enhanced ion–ion interactions and the formation of ion clusters that limit long-range displacement based on the RDF results.

Referring to the MSD results, we extracted the self-diffusion coefficient of Li^+ ($D_{Li}{}^+$) and $TFSI^-$ ($D_{TFSI}{}^-$); the equation is detailed in the Experimental Section. To ensure statistical reliability, these coefficients were averaged over 5 independent MD simulation runs, presented in Tables S2 and S3 (Supporting Information). As shown in Figure 2b, the $D_{Li}{}^+$ showed a concentration-dependent trend. The $D_{Li}{}^+$ decreased monotonically with increasing salt concentration. It dropped sharply from 8.11×10^{-9} cm^2s^{-1} at 50:1 EO ratio to 7.66×10^{-9} cm^2s^{-1} at 25:1 EO ratio, then decreased more gradually, forming a relatively flat region between 25:1 and 8:1 EO ratios (6.85×10^{-9} cm^2s^{-1} at 10:1 and 6.71×10^{-9} cm^2s^{-1} at 8:1). Beyond this intermediate regime, the diffusivity fell markedly to 3.72×10^{-9} cm^2s^{-1} (5:1) and 2.86×10^{-9} cm^2s^{-1} (2:1), representing an overall ≈2.8-fold reduction between the dilute and concentrated systems. We also calculated $D_{TFSI}{}^-$ using the center of mass of the $TFSI^-$ molecules. In analogy to Li^+, the $D_{TFSI}{}^-$ diffusivity shows a gradual decrease with increasing salt concentration. It drops from 1.71×10^{-8} cm^2s^{-1} at 50:1 to 1.55×10^{-8} cm^2s^{-1} (25:1) and then decreases more slowly to 1.42×10^{-8} cm^2s^{-1} (10:1) and 1.41×10^{-8} cm^2s^{-1} (8:1), indicating a near-plateau behavior at intermediate concentrations. At higher concentrations, $D_{TFSI}{}^-$ declines more sharply, reaching 9.69×10^{-9} cm^2s^{-1} (5:1) and 5.80×10^{-9} cm^2s^{-1} (2:1), consistent with the overall decreasing trend of $D_{Li}{}^+$ as a function of ion content. It is

© 2025 Wiley-VCH GmbH

16163028, 2026, 24, Downloaded from https://advanced.onlinelibrary.wiley.com/doi/10.1002/adfm.202517100 by University Of Notre Dame, Wiley Online Library on [11/07/2026]. See the Terms and Conditions (https://onlinelibrary.wiley.com/terms-and-conditions) on Wiley Online Library for rules of use; OA articles are governed by the applicable Creative Commons License

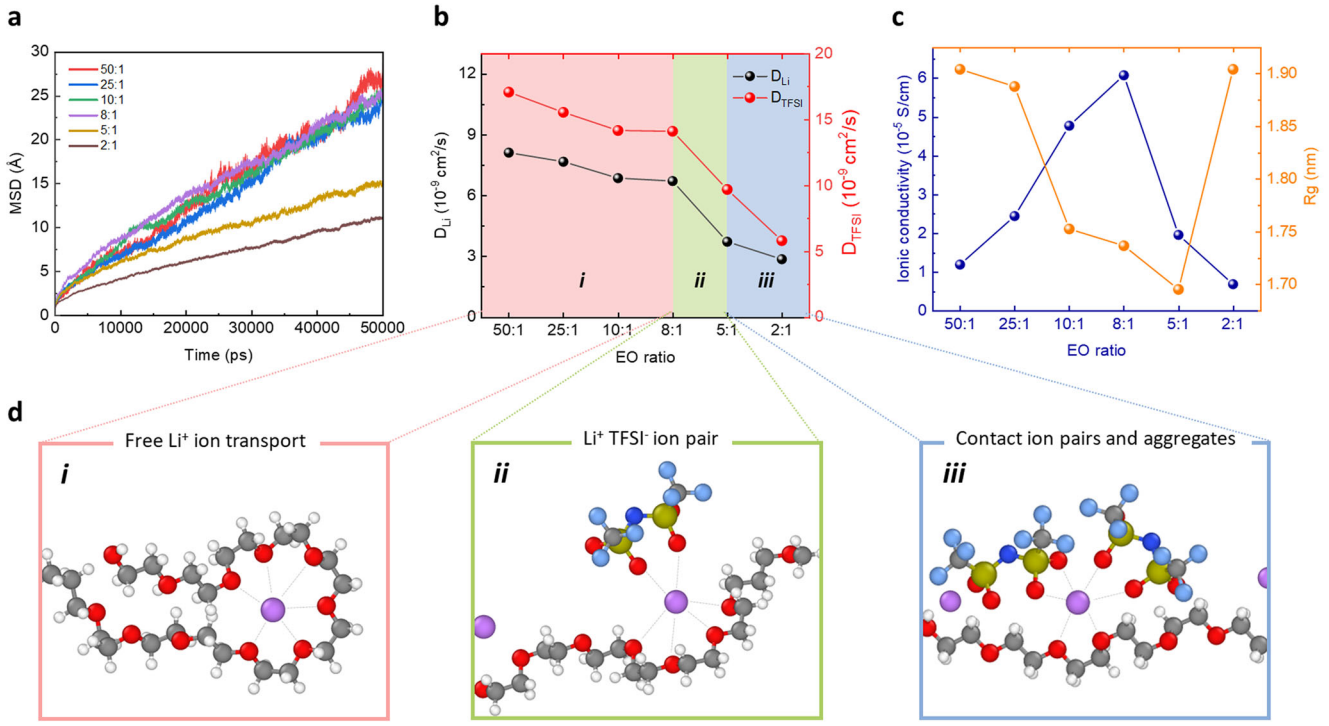


Figure 2. Li^+ displacement, D, and polymer morphology as a function of EO ratio. a) MSD trajectories of Li^+ sampled every 1000 steps over 50 ns and averaged over 5 independent runs, illustrating sub-diffusive behavior at short times and a transition to linear diffusion at long times. b) D_{Li+} (black) and D_{TFSI}^- (red) extracted from the long-time slopes of the MSD curves. c) σ_{Li+} (blue, left axis) and PEO R_g (orange, right axis) plotted versus EO ratio. d) Representative MD snapshots showing Li^+ coordination environments in three concentration regimes: Regime *i* (50:1–8:1), free Li^+ transport with PEO coordination only; Regime *ii* (5:1), formation of Li^+–$TFSI^-$ ion pairs; Regime *iii* (2:1), contact ion pairs and aggregates with overcrowded coordination.

noticeable that D_{TFSI}^- exceeds the corresponding D_{Li}^+ values, which is attributed to the weaker coordination and weaker Coulombic binding of $TFSI^-$ to EO, leading to less steric hindrance and more facile hopping pathways.[37]

In addition to the *D*, we calculated ionic conductivity of Li^+ (σ) via the Nernst–Einstein equation to capture the collective transport behavior and directly relate our simulation data to experimentally measurable performance metrics, as follows:

$$\sigma = \frac{Nq^2}{VkT} D \tag{2}$$

where *V* denotes the total system volume, *N* the number of mobile Li^+, *q* the charge per mobile ion, *T* the absolute temperature, *k* the Boltzmann constant, and *D* the diffusion coefficient of Li^+.[44] While the *D* captures single-ion mobility, the σ reflects ion concentration and correlated motion at higher loadings. Here, σ values were averaged from 510 independent production runs in MD simulations (Table S4, Supporting Information); these values are compared to experimental impedance measurements to validate the reliability of the simulations and force field, and to link atomistic behavior to device performance. In Figure 2c, the σ increases from 1.19×10^{-5} S/cm at 50:1 to a maximum of 6.08×10^{-5} S/cm at 8:1, then decreases to 1.96×10^{-5} S/cm at 5:1 and 6.86×10^{-6} S/cm at 2:1, indicating a clear inflection at the 8:1 EO ratio, consistent with the trend observed in *D* values. Specifically, at the 8:1 EO ratio, the simulated ionic conductivity ($\sigma_{sim} = 6.08 \times 10^{-5}$ S/cm) is comparable to the previously reported value of 7.85×10^{-5} S/cm, confirming the reliability of the suggested simulation protocol.[16] Additional simulations at intermediate EO ratios of 7:1 and 6:1 were performed to further investigate the transition behavior observed at the 8:1 EO ratio (Figure S4, Supporting Information).

Subsequently, we calculated the 10 average R_g of PEO as a function of ion concentration, as summarized in Table S5 (Supporting Information).[45] Figure 2c exhibits a monotonic decrease as the ion concentration increased from 50:1 to 8:1. It can be attributed to the increasing Li^+—EO coordination: as more Li^+ ions bind to the EOs, which can be on the same PEO chain, the Li^+ draws the segments of a chain into tighter conformations and reduces the overall coil size of PEO backbones. Up to the 5:1 composition, the "ion-bridging" effect dominates, leading to progressively lower R_g values from 1.904 Å (50:1) down to 1.695 Å (5:1). Beyond this concentration, however, the onset of ion pairing and clustering—as well as the attendant disruption of local packing—begins to outweigh chain contraction, eventually allowing the polymer chains to re-expand to 1.904 Å at 2:1 ratio.[46]

In MD simulations, the PEO chain conformation changed non-monotonically with ion concentrations. Between 50:1 and 8:1 ratio, increasing Li^+ raises the free-ion population and yields a dominant $Li—O_{PEO}$ RDF peak at 2.125 Å with an average CN of six, accompanied by a decreased R_g that reflects chain

© 2025 Wiley-VCH GmbH

16163028, 2026, 24, Downloaded from https://advanced.onlinelibrary.wiley.com/doi/10.1002/adfm.202517100 by University Of Notre Dame, Wiley Online Library on [11/07/2026]. See the Terms and Conditions (https://onlinelibrary.wiley.com/terms-and-conditions) on Wiley Online Library for rules of use; OA articles are governed by the applicable Creative Commons License

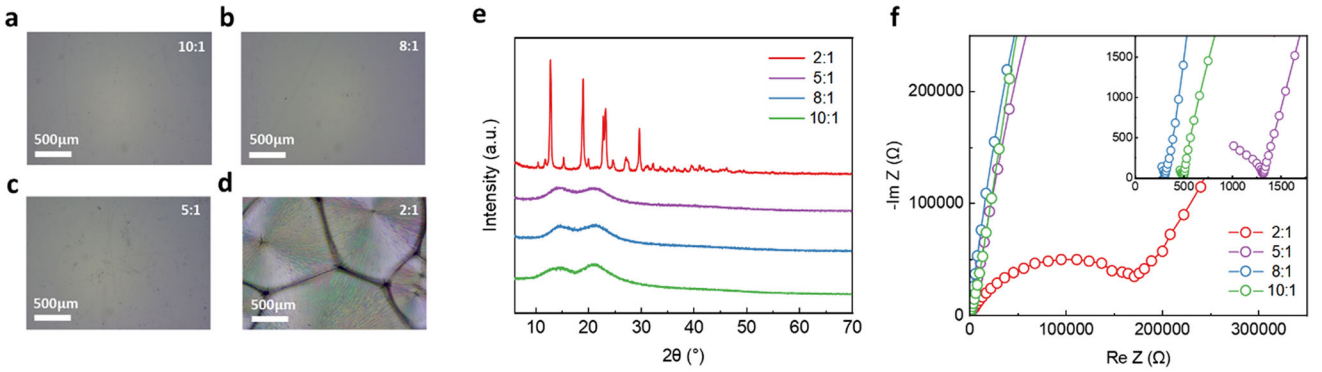


Figure 3. Salt concentration-dependent crystallinity and σ of PEO/LiTFSI electrolytes. OM images of PEO/LiTFSI films at EO ratios of a) 10:1, b) 8:1, c) 5:1, and d) 2:1. e) XRD patterns of PEO/LiTFSI films at various EO ratios (10:1, 8:1, 5:1, and 2:1). f) Nyquist plots of EGTs with different EO ratios. EIS measurements were performed over a frequency range of 100 mHz to 1 MHz. The device used for EIS measurement had a sandwiched MISM structur e (ITO/PEO electrolyte/ZnO/ITO). Insets show the high-frequency region of the EIS spectra.

contraction (Figure 2d,i). In this low-to-intermediate regime, disrupted PEO crystallinity plasticizes the polymer and promotes more frequent intra- and interchain Li^+ hopping via segmental motion. However, at high concentration regimes (from 5:1 to 2:1 EO ratio), this trend reverses. The RDF displays two distinct peaks in $Li—O_{TFSI}^-$: the first at ≈2.175 Å, reflecting bidentate coordination via two $TFSI^-$ oxygens, and another ≈4.425 Å, indicative of monodentate coordination through a single oxygen.[25,47] In super-concentrated PEO/LiTFSI (EO:Li ≤ 5:1), extensive ion–ion pairing and the formation of large aggregates (Figure 2dii,iii) introduce steric barriers that give rise to an MSD plateau and a dramatic decline in Li^+ conductivity, even as the R_g partially rebounds. This aggregation-induced suppression of segmental-motion–driven hopping effectively quenches the intrinsic diffusive behavior of Li^+ and may alleviate the exponential ion dynamics, as necessary for linear weight updates in EGTs.

2.3. Experimental Analysis of Mechanical and Ionic Properties of PEO/LiTFSI

Guided by the MD simulations' insights into how ion coordination and dynamics vary with concentration, we performed experimental validation using four representative EO:Li ratios—10:1, 8:1, 5:1, and 2:1. For each composition, we prepared PEO/LiTFSI electrolytes and fabricate side-gated EGTs (see Experimental Section for details). These specific ratios were chosen to target the key transitional regimes highlighted by simulation and to directly compare simulation predictions with macroscopic device performance. As shown in **Figure** 3a–d, the OM reveals that PEO/LiTFSI electrolytes remain fully amorphous at 10:1, 8:1, and 5:1 EO ratios, with no evidence of crystalline domains. In contrast, the 2:1 sample exhibits extensive crystallization throughout the film, forming characteristic lamellar spherulites. These spherulites nucleate at discrete sites and grow radially until adjacent domains impinge, producing well-defined boundaries. Such radially aligned lamellar structures and spherulitic morphologies are emblematic of PEO's secondary crystallization behavior.[48,49]

At ultrahigh ion concentrations, LiTFSI cluster size and abundance increase remarkably, inducing correlated ion–ion interactions that compete with PEO ether-oxygen coordination.[50] Reduced Li—EO coordination thus restores sufficient polymer chain mobility and interchain packing, permitting pure PEO lamellae to recrystallize within the remaining amorphous matrix.[51] Referring to the OM images, XRD analysis was further conducted to verify the crystallinity and phase composition of the PEO/LiTFSI electrolytes (Figure 3e). PEO/LiTFSI electrolytes at EO ratios of 10:1, 8:1, and 5:1 display a broad diffraction pattern, confirming their amorphous character—consistent with LiTFSI's plasticizing effect that disrupts PEO crystallinity and lowers its glass transition.[52] In contrast, the 2:1 sample exhibits sharp reflections at $2\theta = 19.04°$ and 23.30°, assignable to the (120) and (112) planes of crystalline PEO, indicating re-crystallization under super-concentrated conditions.[53] In addition, the intense peaks observed at 2θ values of 12.86°, 15.36°, 20.08°, 24.76°, 27.20°, and 29.70° indicate the coexistence of crystalline LiTFSI and PfEO/LiTFSI complex phases, demonstrating that specific salt stoichiometry promotes PEO recrystallization and the formation of LiTFSI-containing crystalline complexes.[54,55] Although the PEO/LiTFSI electrolytes are highly crystalline with well-ordered lamellae at 2:1 EO ratio, amorphous domains inevitably reside between lamellae and are interconnected by tie chains.[56,57] These amorphous regions remain well above the T_g of PEO and form a continuous rubbery matrix that accommodates strain. In addition, while high crystallinity in free-standing PEO films is often associated with brittle fracture, substrate-supported, thin, and locally patterned PEO/LiTFSI electrolytes suppress crack initiation and propagation, with the low-T_g amorphous matrix providing mechanical compliance. To investigate the influence of mechanical-property changes in the PEO/LiTFSI electrolyte on the ion transport, σ was calculated from EIS measurements using Equation (3)

$$\sigma = \frac{1}{R_b} \frac{l}{A} \tag{3}$$

where R_b, A, and l represent bulk resistance, area, and thickness of the electrolyte film, respectively.[16] Using R_b values from the Nyquist plots (Figure 3f; Table S6, Supporting Information), σ varies with EO ratios: 4.75×10^{-5}, 7.85×10^{-5}, 1.54×10^{-5}, and

© 2025 Wiley-VCH GmbH

16163028, 2026, 24, Downloaded from https://advanced.onlinelibrary.wiley.com/doi/10.1002/adfm.202517100 by University Of Notre Dame, Wiley Online Library on [11/07/2026]. See the Terms and Conditions (https://onlinelibrary.wiley.com/terms-and-conditions) on Wiley Online Library for rules of use; OA articles are governed by the applicable Creative Commons License

16163028, 2026, 24, Downloaded from https://advanced.onlinelibrary.wiley.com/doi/10.1002/adfm.202517100 by University Of Notre Dame, Wiley Online Library on [11/07/2026]. See the Terms and Conditions (https://onlinelibrary.wiley.com/terms-and-conditions) on Wiley Online Library for rules of use; OA articles are governed by the applicable Creative Commons License

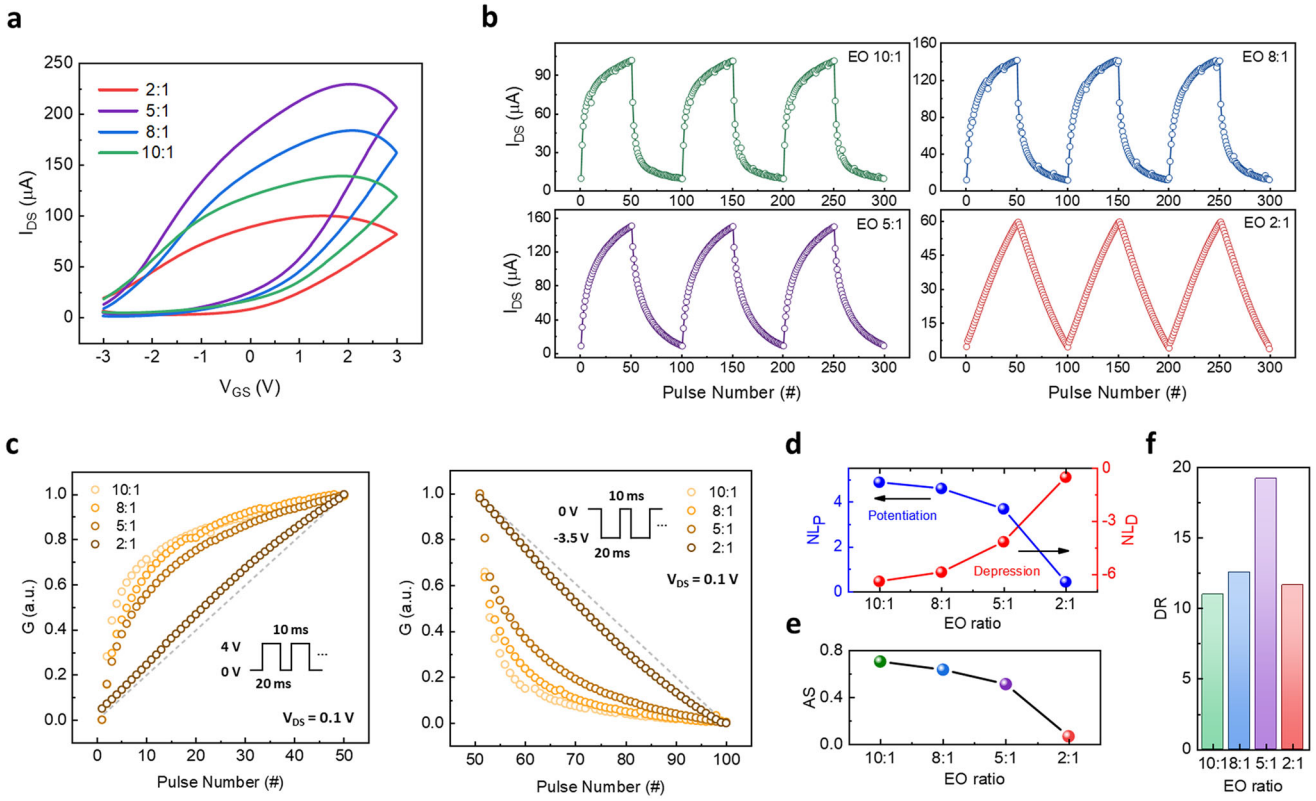


Figure 4. Electrical synaptic characteristics of Li-EGTs with different ion concentrations. a) Transfer curves of Li-EGTs with four different EO ratios (10:1, 8:1, 5:1, and 2:1) plotted on a linear scale at a fixed sweep rate of 0.8 Vs^{-1} (V_{GS} = −3 to 3 V, V_{DS} = 0.1 V). b) Analog conductance modulation characteristics of Li-EGTs with different EO ratios. A total of 50 potentiation and depression pulses were applied over three cycles for each EGT. The pulse parameters are provided in Figure 4c. c) Normalized channel conductance values of Li-EGTs with different EO ratios under consecutive square pulse stimulation. The values of V_{DS} and pulse conditions are indicated in the figure. d) NL parameters for the LTP and LTD regions, shown in blue and red, respectively (ideal NL = 0), for the Li-EGTs with different EO ratios. e) AS parameters corresponding to the different EO ratios. f) Calculated DR under 50 consecutive pulses for the different EO ratios.

1.40×10^{-7} S·cm^{-1} for 10:1, 8:1, 5:1, and 2:1 EO ratio, respectively. The $\sigma_{Li}{}^{+}$ values for four EO ratio conditions, obtained from MD simulations and EIS experimental measurements, are presented in Table S7 (Supporting Information). In both simulation and experiment, the $\sigma_{Li}{}^{+}$ initially increases with ion concentration, peaks at the 8:1 ratio, then decreases as concentration rises further. Excellent agreement was observed at EO ratios of 10:1, 8:1, and 5:1 EO ratios ($\sigma_{Li}{}^{+}{}_{sim}$ = 4.77 × 10^{-5}, 6.08 × 10^{-5}, and 1.96 × 10^{-5} S/cm, respectively) while at high salt concentrations, the simulated $\sigma_{Li}{}^{+}$ was ≈50 times higher than the experimental values ($\sigma_{Li}{}^{+}{}_{sim}$ = 6.86 × 10^{-6} S/cm at 2:1 EO ratio). The deviation likely arises from limitations of the non-polarizable OPLS-AA force field, which cannot fully capture dynamic and local polarization fluctuations in highly concentrated polymer systems. Thus, further optimization using a polarizable force field is required to improve predictive accuracy. Nevertheless, the overall concentration-dependent trend shows excellent qualitative agreement with experiments, validating the predictive capability of MD simulations for electrolyte design. MD simulations reveal that $D_{Li}{}^{+}$ decreases sharply at the 5:1 ratio, as indicated by MSD (Figure 2a). CN analysis also confirms that Li^+ forms coordination bonds with $TFSI^-$ oxygen atoms at this EO ratio. As the system approaches solute saturation, undissociated ion pairs form through electrostatic interactions, reducing Li^+ coordination with EO groups and decreasing σ without phase transition. However, ordered crystallites and ion aggregates dominate the PEO electrolyte at the 2:1 ratio, fundamentally changing the transport mechanism from vehicular motion to ion hopping, which reflects reduced chain flexibility. In the amorphous state, ions move more freely due to greater polymer chain segmental motion.[58] Conversely, Li^+ in the crystalline state must hop between coordination sites within the crystal lattice, requiring a higher activation energy due to the rigid PEO polymer, which significantly changes diffusive ion dynamics into constant motion.[59]

2.4. Artificial Synaptic Characteristics of Li-EGTs

To evaluate the artificial synaptic properties of the Li-EGTs, we test devices with four different EO ratios using a double gate-voltage sweep from −3 to 3 V (V_{DS} = 0.1 V, sweep rate = 0.8 V/s). As shown in **Figure 4a**, all EGTs exhibit hysteresis behavior with substantial memory windows: 3.15 V (10:1), 3.24 V (8:1), 3.45 V (5:1), and 3.39 V (2:1), attributed to mobile ion migration within the PEO/LiTFSI electrolyte. The EGT with 5:1 EO ratio

© 2025 Wiley-VCH GmbH

demonstrates the highest on-state current (I_{DS}). We measured areal capacitance values using a metal-insulator-metal structure (Figure S5, Supporting Information): 1.35, 1.48, 1.62, and 0.405 μFcm^{-2} for the 10:1, 8:1, 5:1, and 2:1 ratios, respectively, with maximum capacitance at 5:1. The obtained capacitance values fall within the typical range for EGTs (1–10 μF cm^{-2}) originating from electric double-layer formation at the electrolyte/semiconductor interface, and are in good agreement with previously reported values.[9,60–62] These results indicate that despite reduced Li^+ diffusivity at 5:1 EO ratio (due to enhanced electrostatic interactions and lower proportion of free Li^+), the larger absolute number of charge carriers—combined with active polymer segmental motion in the amorphous phase—compensates for limited diffusivity. It produces significantly higher I_{DS} compared to other concentrations, suggesting the increased I_{DS} is primarily driven by carrier density rather than ion diffusivity. We also analyzed the imaginary capacitance (C″) from EIS to elucidate ion relaxation and dielectric properties of each PEO/LiTFSI electrolyte. The relaxation time ($\tau = \frac{1}{2\pi f}$) increases with salt concentration from 85.8 μs (10:1), 279 μs (8:1), and 1.34 ms (5:1) to 7.25 s (2:1). Additionally, ion transport changes notably at the 2:1 EO ratio, as described in detail in Figure S5c and the Supporting Notes (Supporting Information).

We conducted analog conductance modulation measurements by applying consecutive 50-pulse voltages to each EGT, as shown in Figure 4b. The repetitive LTP and LTD results demonstrate high tunability across all EO ratios. The LTP and LTD occur through a two-step mechanism: under positive gate bias, Li^+ migrates toward the ZnO channel side and forms an EDL at the ZnO/electrolyte interface, which accelerates electron accumulation in the ZnO channel. Subsequently, Li^+ penetrates into the ZnO thin film due to its small ionic radius (76 pm) and electrochemically dopes the deeper region of ZnO via reversible Faradaic reactions triggered by the applied pulses.[16] The Li-EGTs thereby enable modification of channel conductance and stable long-term memory behavior. To testify to reliability under extreme conditions, we extended testing to 1000 cycles. Figures S6 and S7 (Supporting Information) demonstrate excellent reproducibility with minimal variation under ambient conditions. The cycle-to-cycle variation (CCV) remains below 1.72% across all devices (specifically 1.31%, 1.48%, 1.72%, and 0.12% for EO ratios of 10:1, 8:1, 5:1, and 2:1, respectively). Device-to-device variation (DDV) is also well-controlled at 4.37%, 2.42%, 2.61%, and 3.82% for the corresponding ratios, with a maximum overall variation of 4.37% (Figure S8, Supporting Information). These results confirm the high uniformity and stability of our EGTs across both temporal and spatial scales.

By fitting the LTP/LTD measurement data with normalized channel conductance values, we compared weight update linearity as a function of ion concentration (Figure 4c). The conductance modulation linearity correlates strongly with the underlying ion transport mechanism. At low salt concentrations (10:1–5:1), fully dissociated Li^+ binds with EO segments and follows the polymer's flexible segmental motion in the amorphous phase, resulting in diffusive and exponential conductance changes. In contrast, at high concentration (2:1), recrystallization occurs and ion transport shifts to a hopping-dominated transport between fixed coordination sites with higher activation energy, leading to more stable and controllable conductance modulation, improving linearity.[63]

We further quantified the applicability of each EGT for neuromorphic computing by calculating three key metrics: NL, asymmetry (AS), and dynamic range (DR) (details of NL and AS are in Figure S9, Supporting Information). Ideally, the NL and AS are zero for neuromorphic computing tasks, and wide DR ($G_{max}/G_{min} \geq 10$) enables high-precision synaptic weight representation and updates, reducing quantization error and improving learning accuracy and stability.[64] The EGTs with 2:1 EO ratio achieved the best overall performance, with NL_P and NL_D values of 0.42 and −0.5—closest to the ideal of zero—and an AS of 0.068, which is more than an order of magnitude lower than the 0.707 observed at 10:1 ratio. In other conditions, 10:1, 8:1, and 5:1 EO ratios, the NL values in both potentiation and depression exceeded |3.5|, and AS becomes higher (Figure 4d,e; Table S8, Supporting Information). This phenomenon stems from the intrinsic exponential transport characteristics of carrier ions in EGTs, driven by segmental–motion–mediated Li^+ diffusion. Figure 4f represents that all EGTs exceeded the threshold DR of 10 (10.97 at 10:1, 12.56 at 8:1, 19.19 at 5:1—the highest—and 11.64 at 2:1 ratio). These results demonstrate that all EGTs achieved sufficiently wide DR for neuromorphic computing, and the 2:1 EO ratio exhibits the optimal combination of key performance metrics due to the shift in ion dynamics toward hopping-dominated conduction, despite its lower σ.

2.5. Neuromorphic Computing with EGTs for CNN-Based Recognition Tasks

To assess the neuromorphic computing potential of Li-EGTs, recognition task simulations were conducted using a CNN trained on the CIFAR-10 dataset, which comprises 10 image categories (e.g., truck, airplane, horse) composed of 32 × 32 pixel RGB images (**Figure 5a**). The CNN architecture consists of eight layers, including convolutional, pooling, and fully connected layers, with synaptic weights modulated according to the conductance update characteristics of Li-EGTs as shown in Figure 4.[65,66] As illustrated in Figure 5a, the network processes image features through repeated convolution and pooling operations before reaching the fully connected layers, where the Li-EGT arrays emulate synaptic connections (Figure 5b). Training was performed over 256 epochs using 50 000 images, and 10 000 images were used for inference in each epoch. The simulation setup and circuit implementation are described in detail in the Experimental section.

As shown in Figure 5c, the Li-EGT-based CNN under the 2:1 EO ratio condition achieves a maximum inference accuracy of 89.51%, which is close to the ideal device accuracy of 90.93%. In contrast, simulations at EO ratios of 10:1, 8:1, and 5:1 fail to yield valid results by showing NaN (not a number) due to excessive NL, which impeded proper weight training.[65] The high accuracy at a 2:1 EO ratio is attributed to the excellent linearity ($NL_P = 0.42$, $NL_D = -0.5$) and large DR (11.64) with small variations (CCV = 0.12%, DDV = 3.82%) of conductance modulation in Li-EGTs. These results demonstrate that Li-EGT exhibits the best synaptic performance under the 2:1 EO ratio condition, a

© 2025 Wiley-VCH GmbH

16163028, 2026, 24, Downloaded from https://advanced.onlinelibrary.wiley.com/doi/10.1002/adfm.202517100 by University Of Notre Dame, Wiley Online Library on [11/07/2026]. See the Terms and Conditions (https://onlinelibrary.wiley.com/terms-and-conditions) on Wiley Online Library for rules of use; OA articles are governed by the applicable Creative Commons License

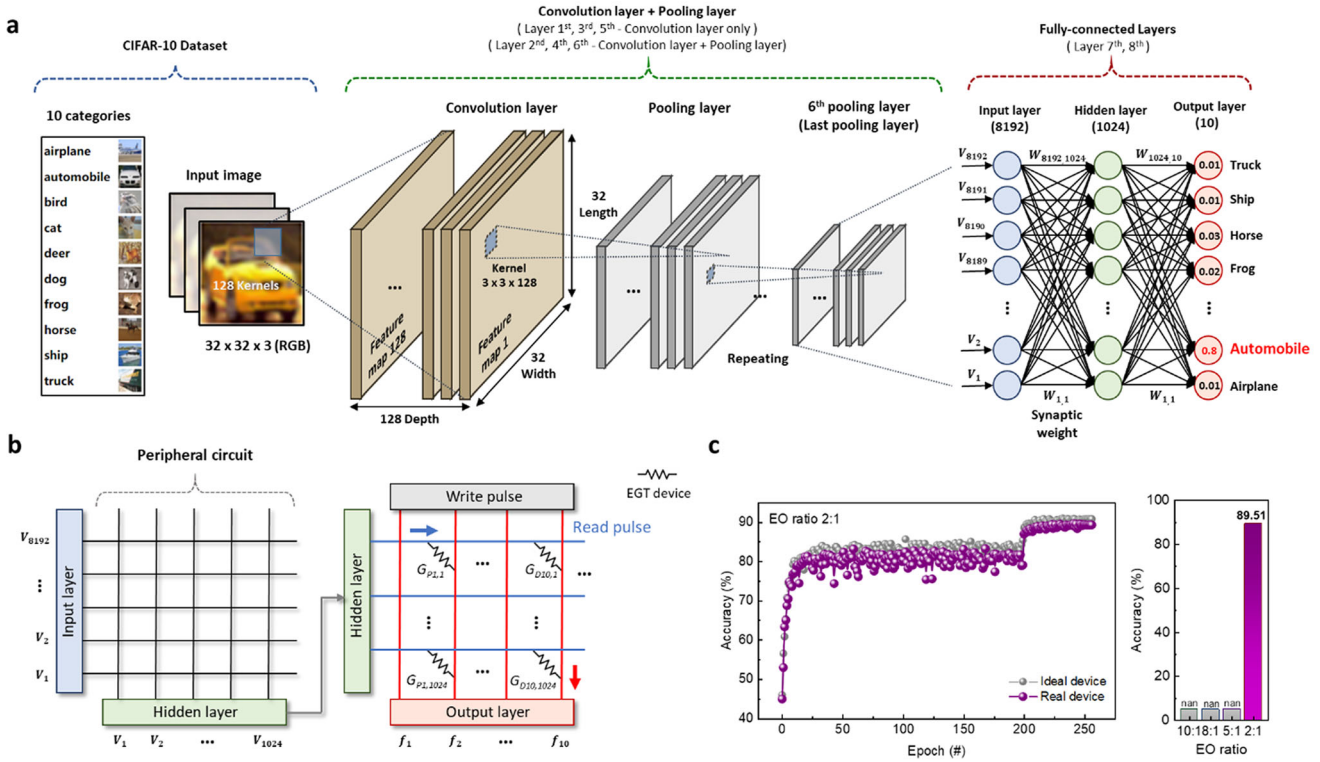


Figure 5. Neuromorphic computing for training and inference tasks using a CNN on the CIFAR-10 dataset. a) Sample images from the CIFAR-10 dataset and the architecture of a CNN consisting of convolutional, pooling, and fully connected layers, trained on the CIFAR-10 dataset for image classification. The dataset image is reprinted from Ref. [76] b) Circuit diagram of a hardware neural network based on Li-EGTs, showing fully connected layers with synaptic arrays and peripheral circuits for implementing write and read pulses in a CNN. c) Inference accuracy results for the CIFAR-10 dataset using EGT-based synaptic arrays. (Left) Accuracy evolution over 256 training epochs for EGTs with an EO ratio of 2:1, comparing ideal (gray) and experimentally measured (purple) characteristics. (Right) Inference accuracy results comparison across different EO ratios.

fundamental shift in the ion transport mechanism from fast segmental-motion-driven diffusion to slower hopping-dominated transport.

3. Conclusion

EGTs are promising artificial synapses, emulating synaptic plasticity, long-term retention, and analog conductance modulation via ion drift/diffusion mechanisms similar to biological neural systems. Especially, understanding ion dynamics in EGTs is essential for high-performance neuromorphic computing, as linear conductance control enables consistent weighted synaptic operations in neural networks. However, macroscopic electrical techniques cannot resolve sub-nanosecond ion transport and depend on iterative, resource-intensive optimization. Here, we combine MD simulations with experiments—using the OPLS-AA force field—to probe femtosecond-resolved Li^+ trajectories in PEO electrolytes at various concentrations. MSD, RDF, and R_g analyses show Li^+ diffusivity decreases above an [EO]:[Li^+] ratio of 8:1, driven by ion-pair/cluster formation and PEO R_g expansion. We validate these simulation results by fabricating EGTs by selecting four conditions (10:1, 8:1, 5:1, and 2:1 ratios). Experimental ionic conductivity drops at 8:1 ratio, and a phase transition at an ultrahigh EO ratio of 2:1 is confirmed via EIS, OM, and XRD. The EGTs with 2:1 electrolyte demonstrate near-ideal multilevel conductance linearity (NL_P = 0.42, NL_D = –0.5), achieving 89.51% accuracy on CIFAR-10. This integrated simulation–experiment approach reveals that linear–symmetric conductance in EGTs requires hopping-dominated Li^+ transport rather than segmental motion—achieved by precise tuning of [EO]:[Li^+] ratios to induce PEO phase transitions—and thus guides the design of high-performance artificial synaptic EGTs.

4. Experimental Section

MD Simulation: The general procedure for the data related to ion dynamics was generated using high-throughput MD simulation. The MD simulations in this work were conducted using the LAMMPS package on a parallel Linux cluster in the Center for Research Computing.[67] The results were visualized using OVITO, and the initial molecular structure setup was conducted with the Materials Studio 2017 software. PEO/LiTFSI complex electrolytes were characterized using the OPLS-AA force field, and the coefficient parameters of PEO polymer and LiTFSI salts were determined by ref. [29,68,69] For all dynamics runs, the temperature was controlled using the Nosé–Hoover thermostat, and the pressure was controlled with the Nosé–Hoover barostat. The Lennard–Jones (LJ) and Coulomb potentials were combined to compute pair interactions between atoms. The particle–particle–mesh (PPPM) k-space solver was used to address the long-range columbic interactions with a relative accuracy of 10^{-4}.[70]

All-atom molecular dynamics simulations were performed in LAMMPS using the real-unit system and full-atom style. Initially, energy minimization was performed to eliminate any unfavorable atomic overlaps. This was

© 2025 Wiley-VCH GmbH

16163028, 2026, 24, Downloaded from https://advanced.onlinelibrary.wiley.com/doi/10.1002/adfm.202517100 by University Of Notre Dame, Wiley Online Library on [11/07/2026]. See the Terms and Conditions (https://onlinelibrary.wiley.com/terms-and-conditions) on Wiley Online Library for rules of use; OA articles are governed by the applicable Creative Commons License

achieved using the conjugate gradient algorithm in LAMMPS, with energy and force convergence criteria set to 10^{-6} and 10^{-7}, respectively. Following the minimization, the PEO/LiTFSI electrolyte system was equilibrated in the canonical ensemble (NVT) at 100 K for 2 ps (using a 0.1 fs timestep) and heated from 100 to 800 K under NVT conditions with a 1 fs timestep over a total simulation time of 5 ns. Subsequently, an isothermal–isobaric (NPT) equilibration was performed at 800 K and a pressure of 1 atm for 50 ps, followed by a pressure ramp from 1 to 500 atm over 2 ns while maintaining the temperature at 800 K. An additional NPT equilibration at 800 K for 2 ps was then conducted. Next, the system was cooled down from 800 K to 300 K in the NPT ensemble over 5 ns, and finally, it was equilibrated at 300 K in the NPT ensemble for 8 ns to achieve a converged density before proceeding to production simulations.[71,72]

The RDF, *g(r)*, describes how particle density varies as a function of distance from a reference particle.

$$g_{ab}\ (r) = \frac{V}{N_a N_b}\left(\sum_{i=1}^{N_a}\frac{n_i b\ (r)}{4\pi r^2 \Delta r}\right) \tag{4}$$

In Equation (4), V denotes the volume of the simulation box; N_a and N_b were the total number of atoms of types a and b, respectively; and $n_i b(r)$ was the average number of b atoms found within a spherical shell at distance r from a reference atom.[73]

The MSD was the ensemble-averaged squared distance traveled by a particle from its initial position as a function of time, serving as a quantitative measure of diffusive transport.

$$MSD = \frac{1}{N}\sum_{i=1}^{N}\left|r_i\ (t) - r_i\ (0)\right|^2 \tag{5}$$

where $r_i(t)$ and $r_i(0)$ represent the positions of atom i in the group at time t and at the initial moment, respectively, and N was the total number of atoms in the group.[41]

The 3D D was calculated using the Einstein equation:[74]

$$D = \lim_{t\to\infty} D\ (t) = \lim_{t\to\infty}\frac{\langle MSD\ (t)\rangle}{6t} \tag{6}$$

The MSD trajectories were sampled every 1000 timesteps over a total simulation time of 50 ns, and averaged across 5 independent production runs, each initialized with a distinct velocity seed (see Figure 2; Figure S1, Supporting Information)

Preparation of LiTFSI Dissolved PEO Electrolytes: Poly(ethylene oxide) (Sigma–Aldrich, Mw: 100 000) and lithium bis(trifluoromethanesulfonyl)imide precursor (Tokyo Chemical Industry Co., Ltd.) were dissolved in anhydrous acetonitrile (Sigma–Aldrich) at [EO]:[M^+] ion ratios of 10:1, 8:1, 5:1, and 2:1. The resulting solutions were stirred overnight using a magnetic stirring bar at 60 °C to obtain a uniform precursor.

Preparation of the ZnO Solution: To prepare the ZnO solution, 0.5 M $Zn(NO_3)_2{\bullet}6H_2O$ was dissolved in 15 mL of deionized (DI) water. Then, 2.5 M NaOH in 10 mL of DI water was added to the $Zn(NO_3)_2$ solution. After mixing, the resulting solution was centrifuged five times with DI water at 5000 rpm for 5 min each time. After centrifugation, the precipitate was collected and dissolved in a mixture of 20 mL NH_4OH and 25 mL DI water.

Fabrication of Li-EGTs: The heavily boron-doped P^{++} Si wafers with a thickness of 200 nm, thermally grown SiO_2 were cut into 2.5 cm × 2.5 cm pieces and cleaned by ultrasonication with detergent for 15 min, deionized (DI) water rinsing for 20 min, acetone for 15 min, isopropyl alcohol (IPA) for 15 min, and N_2 gas blowing for 1 min, followed by UVO treatment for 15 min. The prepared ZnO solution was spin-coated at 3000 rpm for 30 s onto the SiO_2/Si substrate. The ZnO-coated substrate was then heated to 300 °C for 1 h under ambient conditions to sinter the ZnO films. The thickness of the ZnO layer was about 6 nm. Using a photomask, the photolithography was performed to pattern the ZnO thin film channel layer. For source, drain, and side gate electrodes, 100 nm of aluminum metal was deposited on the patterned ZnO (width 1600 µm, length 200 µm) by thermal evaporation at 10^{-6} Torr using metal shadow masks. The prepared PEO electrolyte mixture was drop-cast onto the side-gate, source, and drain electrodes, fully covering them using a micropipette. The EGTs were then dried at 60 °C overnight under ambient conditions to evaporate the solvent.

Device Measurement: The transfer characteristics and pulse measurements for synaptic performance of the EGTs were characterized by Keysight 2902B source/measure unit at room temperature in dark conditions. Using an impedance analyzer (VSP, Bio-Logic SAS), EIS using the two-electrode AC impedance method was performed over the range of 100 mHz–1 MHz. The cell for EIS and capacitance measurements was fabricated as a symmetrical sandwich structure using ITO as the electrode (ITO(+)/electrolyte/ZnO/ITO(-)), with an area of 1 cm^2 and an electrolyte thickness of 130 µm. The AC bias of 10 mV was applied to ITO(+).

Material Characterization: The crystallinity of PEO electrolytes was investigated by XRD analysis (D8 DISCOVER, Bruker, Germany) with Cu Kα radiation over a range of 5–90° of 2θ at a step size 0.02° and time/step of 0.3s with 40 kV, 40 mA.

Convolutional Neural Network Simulation: All simulations were carried out using the open-source DNN+ NeuroSim Framework V2.1 on a Linux workstation. A VGG-8 convolutional neural network—comprising six 3 × 3 convolutional layers interleaved with three pooling layers, followed by two fully connected layers—is trained and tested on the CIFAR-10 dataset (32 × 32 RGB images, 10 classes). During each convolutional layer, the synaptic weight kernels are realized by the conductance states of Li-EGT arrays; activations use the ReLU function, and feature maps are down-sampled via max pooling until a 4 × 4 × 512 tensor is flattened and fed into the classifier.[75] Synaptic weights in both convolutional and fully connected layers are updated according to the experimentally measured device non-idealities: NL, DR, number of conductance levels, CCV, and DDV. Training proceeds for 256 epochs, with 50 000 images randomly sampled per epoch and 10 000 images reserved for inference. Learning rates for the final two fully connected layers are optimized separately for each device condition to maximize classification accuracy.

Supporting Information

Supporting Information is available from the Wiley Online Library or from the author.

Acknowledgements

This research was supported by the Basic Science Research Program through the National Research Foundation of Korea (NRF), funded by the Ministry of Science and ICT (MSIT) of Korea (RS-2023-00208273), and the STEAM Research Program through the NRF, funded by MSIT of Korea (RS-2024-00431341).

Conflict of Interest

The authors declare no conflict of interest.

Data Availability Statement

The data that support the findings of this study are available from the corresponding author upon reasonable request.

Keywords

artificial synapses, electrolyte-gated transistors, ion dynamics, linear conductance modulation, molecular dynamics simulation, neural network-based learning

© 2025 Wiley-VCH GmbH

16163028, 2026, 24, Downloaded from https://advanced.onlinelibrary.wiley.com/doi/10.1002/adfm.202517100 by University Of Notre Dame, Wiley Online Library on [11/07/2026]. See the Terms and Conditions (https://onlinelibrary.wiley.com/terms-and-conditions) on Wiley Online Library for rules of use; OA articles are governed by the applicable Creative Commons License

Received: July 4, 2025
Revised: October 29, 2025
Published online: November 13, 2025

[1] K. Roy, A. Jaiswal, P. Panda, *Nature* **2019**, *575*, 607.
[2] M. Vasilopoulou, A. R. bin Mohd Yusoff, Y. Chai, M. A. Kourtis, T. Matsushima, N. Gasparini, R. Du, F. Gao, M. K. Nazeeruddin, T. D. Anthopoulos, Y. Y. Noh, *Nat. Electron.* **2023**, *6*, 949.
[3] Y. Van De Burgt, E. Lubberman, E. J. Fuller, S. T. Keene, G. C. Faria, S. Agarwal, M. J. Marinella, A. Alec Talin, A. Salleo, *Nat. Mater.* **2017**, *16*, 414.
[4] T. Xiong, C. Li, X. He, B. Xie, J. Zong, Y. Jiang, W. Ma, F. Wu, J. Fei, P. Yu, L. Mao, *Science* **2023**, *379*, 6628.
[5] Y. Zou, D. Liu, X. Gan, R. Yu, X. Zhang, C. Gao, Z. Chen, C. Xu, Y. Ye, Y. Hu, T. Guo, H. Chen, *Adv. Mater.* **2025**, 2419245.
[6] D. Marković, A. Mizrahi, D. Querlioz, J. Grollier, *Nat. Rev. Phys.* **2020**, *2*, 499.
[7] F. Torricelli, D. Z. Adrahtas, Z. Bao, M. Berggren, F. Biscarini, A. Bonfiglio, C. A. Bortolotti, C. D. Frisbie, E. Macchia, G. G. Malliaras, I. McCulloch, M. Moser, T. Q. Nguyen, R. M. Owens, A. Salleo, A. Spanu, L. Torsi, *Nat. Rev. Methods Primers.* **2021**, *1*, 66.
[8] Y. Van De Burgt, A. Melianas, S. T. Keene, G. Malliaras, A. Salleo, *Nat. Electron.* **2018**, *1*, 386.
[9] S. H. Kim, K. Hong, W. Xie, K. H. Lee, S. Zhang, T. P. Lodge, C. D. Frisbie, *Adv. Mater.* **2013**, *25*, 1822.
[10] J. Rivnay, S. Inal, A. Salleo, R. M. Owens, M. Berggren, G. G. Malliaras, *Nat. Rev. Mater.* **2018**, *3*, 17086.
[11] S. Dai, X. Liu, Y. Liu, Y. Xu, J. Zhang, Y. Wu, P. Cheng, L. Xiong, J. Huang, *Adv. Mater.* **2023**, *35*, 2300329.
[12] Y. Dai, S. Dai, N. Li, Y. Li, M. Moser, J. Strzalka, A. Prominski, Y. Liu, Q. Zhang, S. Li, H. Hu, W. Liu, S. Chatterji, P. Cheng, B. Tian, I. McCulloch, J. Xu, S. Wang, *Adv. Mater.* **2022**, *34*, 2201178.
[13] D. Kireev, S. Liu, H. Jin, T. P. Xiao, C. H. Bennett, D. Akinwande, J. A. C. Incorvia, *Nat. Commun.* **2022**, *13*, 4386.
[14] X. Liu, C. Sun, Z. Guo, X. Xia, Q. Jiang, X. Ye, J. Shang, Y. Zhang, X. Zhu, R. W. Li, *Adv. Sci.* **2023**, *10*, 2300471.
[15] C. Wang, Y. Li, Y. Wang, X. Xu, M. Fu, Y. Liu, Z. Lin, H. Ling, P. Gkoupidenis, M. Yi, L. Xie, F. Yan, W. Huang, *J. Mater. Chem. C* **2021**, *9*, 11464.
[16] H. Lee, J. Cho, M. Jin, J. H. Lee, C. Lee, J. Kim, J. Lee, J. C. Shin, J. Yoo, E. Lee, Y. S. Kim, *ACS Nano* **2023**, *17*, 13.
[17] D. Devaux, R. Bouchet, D. Glé, R. Denoyel, *Solid State Ion* **2012**, *227*, 119.
[18] Y. Zhang, N. H. C. Lewis, J. Mars, G. Wan, N. J. Weadock, C. J. Takacs, M. R. Lukatskaya, H.-G. Steinrück, M. F. Toney, A. Tokmakoff, E. J. Maginn, *J. Phys. Chem. B* **2021**, *125*, 17.
[19] D. Reber, R.-S. K. ühnel, C. Battaglia, *Sustain. Energy Fuels* **2017**, *1*, 2155.
[20] J. J. N. Lim, G. J. H. Lim, Y. Cai, R. Chua, Y. Guo, Y. Yan, M. Srinivasan, *J. Mat. Chem. A* **2023**, *11*, 22688.
[21] E. Quartarone, P. Mustarelli, *J. Electrochem. Soc.* **2020**, *167*, 050508.
[22] R. I. Pushparaj, A. R. Kumar, G. Xu, *Energy Storage Mater.* **2023**, *72*, 621.
[23] Q. Zheng, D. M. Pesko, B. M. Savoie, K. Timachova, A. L. Hasan, M. C. Smith, T. F. Miller, G. W. Coates, N. P. Balsara, *Macromolecules* **2018**, *51*, 7.
[24] D. J. Brooks, B. V. Merinov, W. A. Goddard, B. Kozinsky, J. Mailoa, *Macromolecules* **2018**, *51*, 8987.
[25] P. Kang, L. Wu, D. Chen, Y. Su, Y. Zhu, J. Lan, X. Yang, G. Sui, *J. Phys. Chem. B.* **2022**, *126*, 4531.
[26] W. Gorecki, M. Jeannin, E. Belorizky, C. Roux, M. Armand, *J. Phys.: Condens. Matter.* **1995**, *7*, 682.
[27] M. Marzantowicz, J. R. Dygas, F. Krok, *Electrochim. Acta* **2008**, *53*, 7417.
[28] A. I. Jewett, D. Stelter, J. Lambert, S. M. Saladi, O. M. Roscioni, M. Ricci, L. Autin, M. Maritan, S. M. Bashusqeh, T. Keyes, R. T. Dame, J. E. Shea, G. J. Jensen, D. S. Goodsell, *J. Mol. Biol.* **2021**, *433*, 166841.
[29] W. Jiang, D. Wang, W. Li, J. Zhang, *Macromolecules* **2024**, *57*, 18.
[30] Ø. Gullbrekken, S. K. Schnell, *New J. Chem.* **2023**, *47*, 20344.
[31] M. Kozdra, D. Brandell, C. M. Araujo, A. Mace, *Phys. Chem. Chem. Phys.* **2024**, *26*, 6216.
[32] B. Doherty, X. Zhong, S. Gathiaka, B. Li, O. Acevedo, *J. Chem. Theory Comput.* **2017**, *13*, 6131.
[33] J. Schmidt, C. Krekeler, F. Dommert, Y. Zhao, R. Berger, L. Delle Site, C. Holm, *J. Phys. Chem. B.* **2010**, *114*, 6150.
[34] K. Wendler, S. Zahn, F. Dommert, R. Berger, C. Holm, B. Kirchner, L. D. Site, *J. Chem. Theory Comput.* **2011**, *7*, 10.
[35] F. Dommert, K. Wendler, R. Berger, L. Delle Site, C. Holm, *ChemPhysChem* **2012**, *13*, 7.
[36] H. Gudla, C. Zhang, *J. Phys. Chem. B.* **2024**, *128*, 10537.
[37] O. Borodin, G. D. Smith, *J. Solution Chem.* **2007**, *36*, 803.
[38] L. T. Costa, M. C. C. Ribeiro, *J. Chem. Phys.* **2006**, *124*, 184902.
[39] S. Li, Z. Cao, Y. Peng, L. Liu, V. Wang, S. Wang, J. Q. Wang, T. Yan, X. P. Gao, D. Y. Song, P. W. Shen, *J. Phys. Chem. B.* **2008**, *112*, 20.
[40] C. Park, M. Kanduč, R. Chudoba, A. Ronneburg, S. Risse, M. Ballauff, J. Dzubiella, *J. Power Sources* **2018**, *373*, 70.
[41] F. Li, B. Xu, X. Geng, S. Guo, S. Wang, D. Li, *Ionics* **2024**, *30*, 145.
[42] H. Gudla, C. Zhang, D. Brandell, *J. Phys. Chem. B.* **2020**, *124*, 8124.
[43] P. Fayon, L. Sarkisov, *Phys. Chem. Chem. Phys.* **2019**, *21*, 26453.
[44] X. He, Y. Zhu, A. Epstein, Y. Mo, *npj Comput. Mater.* **2018**, *4*, 18.
[45] T. Yin, G. Wang, Z. Guo, Y. Pan, J. Song, Q. Ding, G. Zhao, *Lubricants.* **2024**, *12*, 205.
[46] P. Jia, J. Zhao, *J. Chem. Phys.* **2009**, *131*, 231103.
[47] J. Tong, S. Wu, N. von Solms, X. Liang, F. Huo, Q. Zhou, H. He, S. Zhang, *Front. Chem.* **2020**, *7*, 945.
[48] F. J. Baltá-Calleja, T. A. Ezquerra, *In Encyclopedia of Materials: Science and Technology*, Elsevier, **2001**, 7244.
[49] B. Crist, J. M. Schultz, *Prog. Polym. Sci.* **2016**, *56*, 1.
[50] T. Mabuchi, K. Nakajima, T. Tokumasu, *Micromachines* **2021**, *12*, 1012.
[51] M. Marzantowicz, J. R. Dygas, F. Krok, J. L. Nowiński, A. Tomaszewska, Z. Florjańczyk, E. Zygadło-Monikowska, *J. Power Sources* **2006**, *159*, 420.
[52] M. Marzantowicz, J. R. Dygas, F. Krok, A. Łasińska, Z. Florjańczyk, E. Zygadło-Monikowska, A. Affek, *Electrochim. Acta* **2005**, *50*, 3969.
[53] J. Krajenta, M. Polińska, G. Lapienis, A. Pawlak, *Polymer* **2020**, *197*, 122500.
[54] M. Ravi, S. Kim, F. Ran, D. S. Kim, Y. M. Lee, M. H. Ryou, *J. Memb. Sci.* **2021**, *621*, 119018.
[55] R. N. S. Rofika, W. Honggowiranto, H. Jodi, S. Sudaryanto, E. Kartini, R. Hidayat, *Ionics* **2019**, *25*, 3661.
[56] A. Wang, C. Chen, L. Liao, J. Qian, F.-G. Yuan, N. Zhang, *J. Inorg. Organomet. Polym.* **2020**, *30*, 1497.
[57] P. Koziol, K. Kosowska, D. Liberda, F. Borondics, T. P. Wrobel, *J. Am. Chem. Soc.* **2022**, *144*, 14278.
[58] Z. Li, J. Fu, X. Zhou, S. Gui, L. Wei, H. Yang, H. Li, X. Guo, *Adv. Sci.* **2023**, *10*, 2201718.
[59] Q. Zhou, M. Chen, J. Lu, B. Sheng, J. Chen, Q. Zhang, X. Haner, *Mater. Horiz.* **2025**, *12*, 3201.
[60] H. Ling, D. A. Koutsouras, S. Kazemzadeh, Y. van de Burgt, F. Yan, P. Gkoupidenis, *Appl. Phys. Rev.* **2020**, *7*, 011307.
[61] K. Xu, J. Liang, A. Woeppel, M. E. Bostian, H. Ding, Z. Chao, J. R. McKone, E. J. Beckman, S. K. Fullerton-Shirey, *ACS Appl. Mater. Interfaces.* **2019**, *11*, 39.

© 2025 Wiley-VCH GmbH

16163028, 2026, 24, Downloaded from https://advanced.onlinelibrary.wiley.com/doi/10.1002/adfm.202517100 by University Of Notre Dame, Wiley Online Library on [11/07/2026]. See the Terms and Conditions (https://onlinelibrary.wiley.com/terms-and-conditions) on Wiley Online Library for rules of use; OA articles are governed by the applicable Creative Commons License

[62] N.-K. Cho, J. Cho, G. Yoo, J.-e. Huh, S. Lee, S. Kim, S.-Y. Yoon, J. Yoo, Y. S. Kim, *Appl. Phys. Express.* **2019**, *12*, 101004.
[63] C. D. Fang, Y. Huang, Y. F. Sun, P. F. Sun, K. Li, S. Y. Yao, M. Y. Zhang, W. H. Fang, J. J. Chen, *Nat. Commun.* **2024**, *15*, 6781.
[64] M. K. Kim, Y. Park, I. J. Kim, J. S. Lee, *iScience* **2020**, *23*, 101846.
[65] X. Peng, S. Huang, H. Jiang, A. Lu, S. Yu, *IEEE Trans. Comput.-Aided Des. Integr.* **2021**, *40*, 2306.
[66] T. P. Xiao, C. H. Bennett, B. Feinberg, S. Agarwal, M. J. Marinella, *Appl. Phys. Rev.* **2020**, *7*, 031301.
[67] S. Plimpton, *J. Comput. Phys.* **1995**, *117*, 1.
[68] A. Stukowski, *Modelling Simul. Mater. Sci. Eng.* **2010**, *18*, 015012.
[69] S. W. I. Siu, K. Pluhackova, R. A. Böckmann, *J. Chem. Theory Comput.* **2012**, *8*, 1459.
[70] R. W. Hockney, J. W. Eastwood, *Computer Simulation Using Particles*, 1st ed., CRC Press, Boca Raton, **2021**.
[71] S. Tian, Z. Xu, S. Wu, T. Luo, G. Xiong, *Int. J. Heat. Mass. Transf.* **2022**, *195*, 123134.
[72] S. Tian, D. Huang, Z. Xu, S. Wu, T. Luo, G. Xiong, *Int. J. Heat. Mass. Transf.* **2022**, *183*, 122188.
[73] M. Tahiri, A. Hassani, K. Sbiaai, A. Hasnaoui, *Comput. Condens. Matter.* **2018**, *14*, 74.
[74] V. Lesch, Z. Li, D. Bedrov, O. Borodin, A. Heuer, *Phys. Chem. Chem. Phys.* **2016**, *18*, 382.
[75] S. Seo, J.-J. Lee, R.-G. Lee, T. H. Kim, S. Park, S. Jung, H.-K. Lee, M. Andreev, K.-B. Lee, K.-S. Jung, S. Oh, H.-J. Lee, K. S. Kim, G. Y. Yeom, Y.-H. Kim, J.-H. Park, *Adv. Mater.* **2021**, *33*, 2102980.
[76] A. Krizhevsky, G. Hinton, Learning multiple layers of features from tiny images, **2009**, https://www.cs.toronto.edu/~kriz/cifar.html.

© 2025 Wiley-VCH GmbH

16163028, 2026, 24, Downloaded from https://advanced.onlinelibrary.wiley.com/doi/10.1002/adfm.202517100 by University Of Notre Dame, Wiley Online Library on [11/07/2026]. See the Terms and Conditions (https://onlinelibrary.wiley.com/terms-and-conditions) on Wiley Online Library for rules of use; OA articles are governed by the applicable Creative Commons License